Zitierweise: *Angew. Chem. Int. Ed.* **2025**, *64*, e202424248
doi.org/10.1002/anie.202424248

CO_2 Electroreduction

Interfacial Oxygen Vacancy-Copper Pair Sites on Inverse CeO_2/Cu Catalyst Enable Efficient CO_2 Electroreduction to Ethanol in Acid

Yan Qiao[+], Shenyu Shen[+], Chenghui Mao[+], Yongchun Xiao, Wenchuan Lai, Yanan Wang, Xingyu Zhong, Yangfan Lu, Jiong Li, Jingjie Ge, Hsien-Yi Hsu, Yaqiong Su, Minhua Shao, Zheng Hu,* and Hongwen Huang**

Abstract: Renewable electricity-driven electrochemical reduction of CO_2 offers a promising route for the production of high-value ethanol. However, the current state of this technology is hindered by low selectivity and productivity, primarily due to a limited understanding of the atomic-level active sites involved in ethanol formation. Herein, we identify that the interfacial oxygen vacancy-neighboring Cu (O_v-Cu) pair sites are the active sites for CO_2 electroreduction to ethanol. A linear correlation between the density of O_v-Cu pair sites and ethanol productivity is experimentally evidenced. Moreover, a high Faradaic efficiency of 48.5 % and a partial current density of 344.0 mA cm^{-2} for ethanol production are achieved over the inverse CeO_2/Cu catalyst with a high density of O_v-Cu pair sites in acid. Mechanistic studies that combine density functional theory calculations and spectroscopic techniques propose an O_v-involved mechanism where interfacial O_v sites directly activate and dissociate CO_2 into *CO in a thermodynamically spontaneous manner, thus favoring the subsequent *CHO formation and asymmetric CHO-CO coupling. Besides, the asymmetric O_v-Cu pair sites could preferentially stabilize the *CH_2CHOH intermediate, resulting in the favorable formation of ethanol over ethylene. Our findings provide new atomic-level insights into CO_2 electroreduction to ethanol, paving the way for the rational design of future catalysts.

Introduction

The electrochemical reduction of CO_2 (ECO_2R) into multi-carbon (C_{2+}) products driven by renewable clean electricity presents a promising avenue to upgrade greenhouse gas into value-added chemicals and fuels.[1] Relative to traditional ECO_2R in alkaline/neutral electrolytes, operating ECO_2R in acidic media has recently received great attention because of its unique advantages.[2] On the one hand, acidic electrolyte can inhibit carbonate formation, thereby improving the single-pass carbon efficiency and reducing the energy penalty for (bi)carbonate regeneration.[3] On the other hand,

[*] Y. Qiao,[+] Y. Xiao, W. Lai, Y. Wang, Prof. H. Huang
College of Materials Science and Engineering
Hunan University
Changsha, Hunan 410082, P. R. China
E-mail: huanghw@hnu.edu.cn

S. Shen,[+] Prof. Y. Su
School of Chemistry, Engineering Research Center of Energy Storage Materials and Devices of Ministry of Education, National Innovation Platform (Center) for Industry-Education Integration of Energy Storage Technology
Xi'an Jiaotong University
Xian, Shanxi 710049, P. R. China
E-mail: yqsu1989@xjtu.edu.cn

C. Mao,[+] Prof. Z. Hu
Key Laboratory of Mesoscopic Chemistry of MOE and Jiangsu Provincial Laboratory for Nanotechnology, School of Chemistry and Chemical Engineering
Nanjing University
Nanjing, Jiangsu 210023, P. R. China
E-mail: zhenghu@nju.edu.cn

X. Zhong, Prof. J. Li
Shanghai Synchrotron Radiation Facility, Shanghai Advanced Research Institute
Chinese Academy of Sciences
Shanghai 201210, P. R. China

Y. Lu
School of Materials Science and Engineering, State Key Laboratory of Silicon and Advanced Semiconductor Materials
Zhejiang University
Hangzhou, Zhejiang 310027, P. R. China

Prof. J. Ge
Department of Applied Biology and Chemical Technology
The Hong Kong Polytechnic University
Kowloon, Hong Kong 999077, P. R. China

Prof. H.-Y. Hsu
School of Energy and Environment, Department of Materials Science and Engineering, Centre for Functional Photonics (CFP)
City University of Hong Kong
Kowloon, Hong Kong 999077, P. R. China

Prof. M. Shao
Department of Chemical and Biological Engineering
The Hong Kong University of Science and Technology
Kowloon, Hong Kong 999077, P. R. China

Prof. H. Huang
Shenzhen Research Institute of Hunan University
Shenzhen, Guangdong 518055, P. R. China

[+] These authors contributed equally to this work.

© 2025 Wiley-VCH GmbH

liquid product crossover (e.g., formic acid and ethanol) due to diffusion, migration, and electro-osmotic drag can be mitigated by utilizing the proton exchange membrane.[4] These characteristics render acidic ECO_2R beneficial for commercializing this technology. To date, a few studies have been dedicated to boosting the activity and selectivity of C_{2+} products in acidic ECO_2R via designing advanced Cu-based catalysts and modulating local reaction environments.[5] Among these C_{2+} products, ethanol (EtOH) is particularly desired due to its high energy density (26.8 MJ/kg), long-term storage, and convenient transport.[6] Unfortunately, it has been found that ethylene is usually the dominant product among C_{2+} products in ECO_2R because of its thermodynamically favored reaction pathway over Cu surface.[7] To our knowledge, the maximal Faradaic efficiency (FE) for ethanol in acidic ECO_2R reported is 40.5 % with a partial current density of 340.2 mA cm^{-2}.[8]

Identifying the atomic-level active site for ethanol production is central to understanding how the catalytic reaction proceeds and to the design of advanced catalysts. For example, the knowledge on the role of Cu^0/Cu^+ sites as the active sites for ECO_2R-to-ethanol has greatly advanced the discovery of remarkable Cu-based catalysts for ethanol production through strategies such as element doping and interface construction.[9] In a notable case, the Cu/BaO interface featuring the mixed Cu^0/Cu^+ sites was designed and constructed for highly selective ECO_2R-to-C_{2+} alcohols.[10] Although some progress has been made, it is undoubtedly desirable to identify the true atomic-level active sites for ethanol production. Mechanistically, it is revealed that the ECO_2R on the Cu sites often faces the high energy barrier for the formation of *CO (or *CHO), limiting the asymmetric C–C coupling kinetics, the key step for C_{2+} production.[11] Besides, the key intermediate $*CH_2CHOH$ for ethanol formation is typically less stable than $*CH_2CH_2O$, which leads to prevalent ethylene formation on Cu sites.[12] As thus, identifying the catalytically active sites with enhanced abilities to promote the *CO (or *CHO) formation and stabilize the $*CH_2CHOH$ is the key direction.

Lattice oxygen vacancies (O_v) have been extensively studied for their role in decreasing the formation barrier of the adsorbed *CO in many catalytic reactions, such as reverse water-gas shift, CO_2 hydrogenation, and photocatalytic CO_2 reduction.[13] Inspired by these, we reasoned that constructing the asymmetric pair sites incorporating Cu and interfacial O_v may promote the *CO/*CHO formation and thereby facilitate ethanol production. Density functional theory (DFT) calculations also predict that the interfacial O_v-Cu pair sites can directly activate and dissociate CO_2 into *CO in a thermodynamically spontaneous manner, in turn facilitating the formation of *CHO and the subsequent asymmetric CHO-CO coupling for ethanol formation. To realize the robust and abundant interfacial O_v-Cu pair sites,[14] we herein delicately designed and constructed an inverse CeO_2/CuO catalyst. The rational for the adoption of CeO_2 lies in the excellent resistance of CeO_2 to corrosion under acidic ECO_2R conditions and its fast kinetics to generate lattice O_v through the reversible switch of $Ce^{3+} \leftrightarrow Ce^{4+}$. Consistent with the DFT predictions, the as-designed inverse CeO_2/CuO catalyst with abundant interfacial O_v-Cu pair sites exhibits a record-high Faradaic efficiency of 48.5 % at a partial current density of 344.0 mA cm^{-2} for ethanol production in acidic electrolyte. Moreover, the active sites of interfacial O_v-Cu pairs were experimentally identified by the nearly linear correlation between the density of interfacial O_v-Cu pair sites and ethanol productivity.

Results and Discussion

Theoretical Predictions

To explore whether the interfacial O_v-neighboring Cu pair sites could facilitate the *CO/*CHO formation and asymmetric CHO-CO coupling for ethanol production, DFT calculations were performed. The model was first constructed via grafting the $Ce_{12}O_{23}$ cluster with an interfacial O_v onto the thermodynamically favorable Cu (111) surface. The model of Cu (111) surface was also employed for comparison (Figure S1). We compared the Gibbs free energy for the formation of *CHOCO on the distinct sites (Figures S2–S4), including the Cu sites on Cu (111) slab (denotes as Cu sites), Cu sites near the $Ce_{12}O_{23}$/Cu interface on the $Ce_{12}O_{23}$/Cu slab (denotes as $Cu_{interface}$ sites), and interfacial O_v-neighboring Cu pair sites on the $Ce_{12}O_{23}$/Cu slab (denotes as O_v-Cu pair sites). Strikingly, it is found that, on the interfacial O_v-Cu pair sites, CO_2 could be directly dissociated into *CO in a thermodynamically spontaneous manner, followed by the protonation of *CO to *CHO with a very low activation energy of 0.21 eV (Figure 1a,b). As contrast, the activation energy required for the formation of *CHO on the Cu sites and $Cu_{interface}$ sites is 0.92 eV and 0.82 eV, respectively, much higher than 0.21 eV on O_v-Cu pair sites. These results indicate that O_v-Cu pair sites can thermodynamically favor the formation of *CO/*CHO intermediate in ECO_2R through an O_v-involved mechanism, similar to the case in thermal/photocatalytic CO_2 hydrogenation.[15] Of note, O_v in electrocatalysts were often reported to regulate the adsorption and desorption energies of neighboring active sites in previous studies,[16] rather than directly participating in the elementary reaction steps. We also find that the CO-CHO coupling, the key process for the formation of C_{2+} products, is an energetically downhill process on all the sites, consistent with the prior studies.[17] These results indicate that the O_v-Cu pair sites have the lowest activation energy for the asymmetric CO-CHO coupling compared to the Cu sites and $Cu_{interface}$ sites, predicting the highest activity of O_v-Cu pair sites for C_{2+} production among these distinct sites. To rationalize the observed trend in activation energy for CO-CHO coupling, we also computed the adsorption energies of *CO, *CHO, and *CHOCO on the different sites (Figure 1c). The result demonstrates that the adsorption of these intermediates is much stronger on the O_v-Cu pair sites than on the Cu sites and $Cu_{interface}$ sites, consistent with the smallest free energy difference for CO-CHO coupling on the O_v-Cu pair sites.

 © 2025 Wiley-VCH GmbH

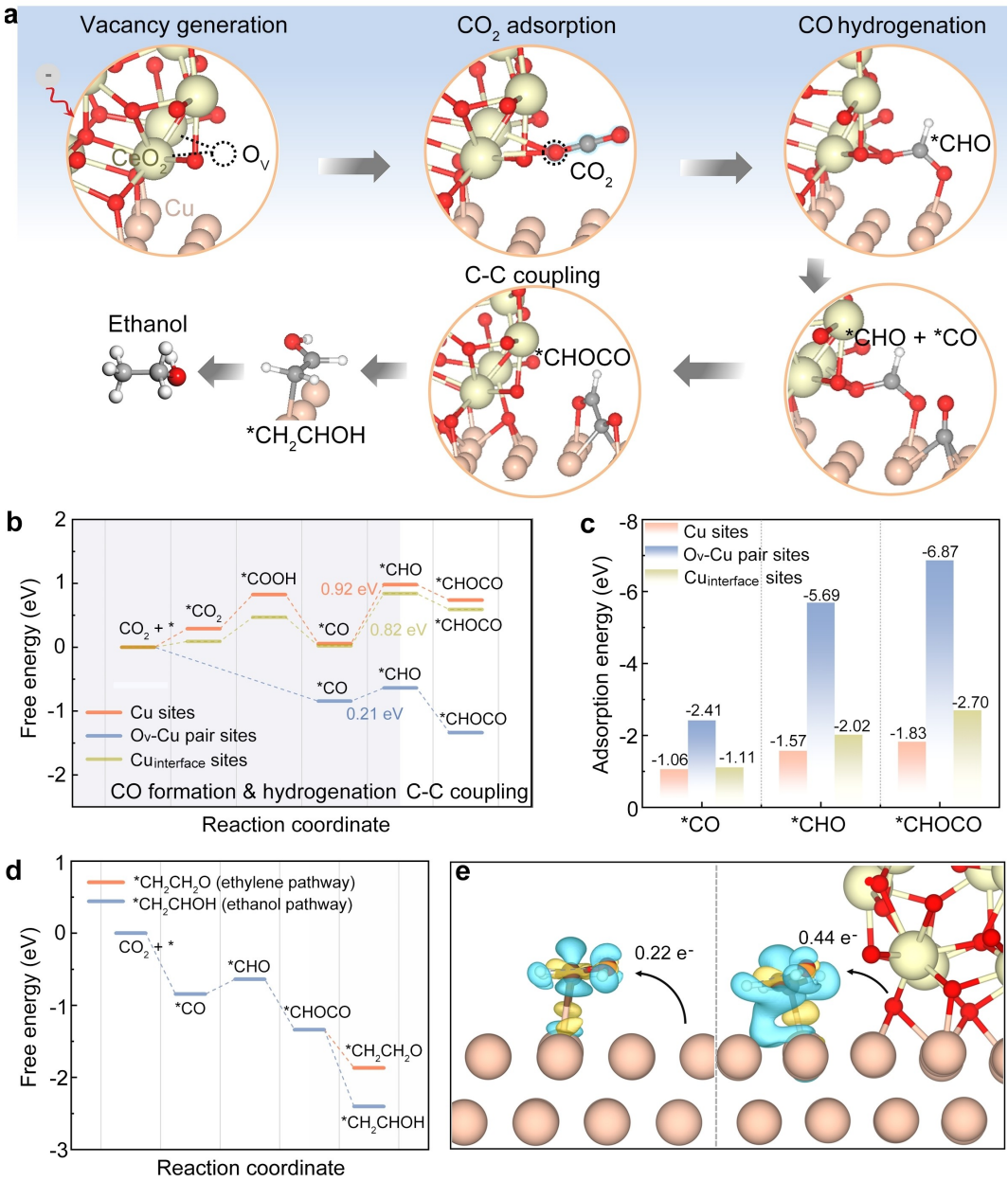

Figure 1. Theoretical calculations. (a) Proposed reaction paths for CO_2 electroreduction to ethanol over $Ce_{12}O_{23}$/Cu slab. Color codes: Cu, pink; Ce, yellow; C, gray; O, red; H, white. (b) The free energy diagram of ECO_2R to ethanol over Cu sites, $Cu_{interface}$ sites, and interfacial O_v-Cu pair sites. (c) The adsorption energy of *CO, *CHO and *CHOCO on different sites. (d) The comparison of free energy for the ethanol and ethylene pathways on interfacial O_v-Cu pair sites. (e) Side view of electronic difference and Bader analysis for Cu (left) and $Ce_{12}O_{23}$/Cu (right). Yellow and blue counters represent the isosurfaces of electronic charge accumulation and depletion, respectively.

Based on the earlier studies, the formation pathways of ethanol and ethylene branch off from the common *CHOCO intermediate.[11b,12] From this branching point, the ethanol pathway proceeds through the $*CH_2CHOH$ intermediate, whereas ethylene formation relies on the $*CH_2CH_2O$ intermediate (Figure S5). Therefore, we calculated the formation energy of two key intermediates (Figure S6). As depicted in Figure 1d, the formation of ethanol is thermodynamically more favored on the O_v-Cu pair sites, while the ethylene pathway is preferred on Cu sites (Figures S7 and S8). To gain insights into the preferential formation of $*CH_2CHOH$ on O_v-Cu pair sites, we analyzed the electronic density difference and Bader charge (Figure 1e). Clearly, the charge shift from O_v-Cu pair sites to $*CH_2CHOH$ (0.44 e) is notably larger than the shift observed on the Cu sites (0.22 e), indicating enhanced stabilization of $*CH_2CHOH$ on the O_v-Cu pair sites. Taken together, DFT calculations predict that the interfacial O_v-Cu pair sites can promote the *CO/*CHO formation, asymmetric CHO-CO coupling, and $*CH_2CHOH$ formation through an O_v-involved mechanism, leading to the thermodynamically favored formation of ethanol over ethylene.

© 2025 Wiley-VCH GmbH

Catalyst Synthesis and Characterizations

Guided by the DFT calculations, we further attempted to design the desired catalyst with the high density of interfacial O_v-Cu pair sites. Experimentally, we delicately used copper oxide (CuO) nanosheets as the host, onto which cerium oxide (CeO_2) nanoislands were grown to create an inverse CeO_2/CuO catalyst with an abundant interface through a two-step immersion-calcination method (Figure S9). The detailed morphology, crystal structure, and composition of the CeO_2/CuO catalyst were meticulously characterized. The transmission electron microscopy (TEM) images reveal that the CeO_2/CuO catalyst preserves the leaf-shaped nanosheet morphology of pure CuO (Figures S10 and S11). Also, a large number of nanocavities with an average diameter of around 17.5 nm could be resolved on CeO_2/CuO. High-angle annular dark-field scanning transmission electron microscopy (HAADF-STEM) images show the increased surface roughness of CeO_2/CuO compared to the pristine CuO (Figure 2a,b). By a closer examination, the alien nanoislands with an average size of 5.3 nm could be observed within the nanocavities of the CeO_2/CuO catalyst (inset in Figure 2b), which is further evidenced by the high-magnification HAADF-STEM image (Figure 2c). We hypothesize that these nanoislands are the CeO_2 that were grafted on the CuO nanosheet through the immersion-calcination synthesis. The Raman spectra (Figure 2d) exhibit the characteristic peaks at 279, 332, 621 and 1103 cm^{-1}, corresponding to A_g, B_{1g}, B_{2g} and $2B_g$ modes of CuO, respectively, for both CuO and CeO_2/CuO catalysts. As expected, an additional peak at 466 cm^{-1} matching with the F_{2g} mode of Ce–O is observed on CeO_2/CuO catalyst. The X-ray diffraction (XRD) pattern (Figure S12) confirms the presence of cubic CeO_2 phase (PDF#75–0390) and monoclinic CuO phase (PDF#45–0937) in CeO_2/CuO catalyst. The atomic-resolution HAADF-STEM image further shows the

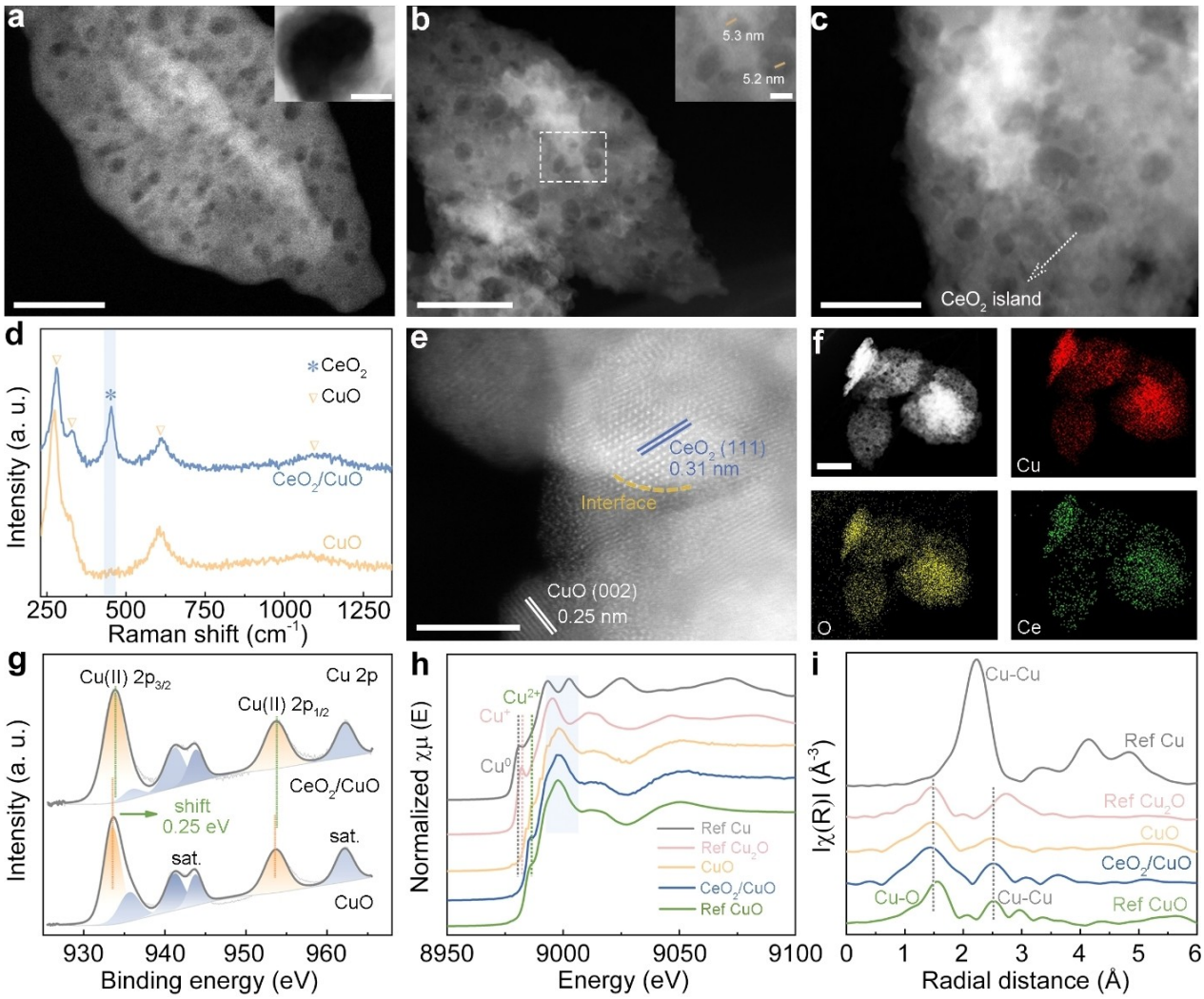

Figure 2. Structural analysis. HAADF-STEM images of CuO (a) and CeO_2/CuO (b, c) nanocatalysts. The inset shows the HAADF-STEM image of nanocavities. Scale bar, a, b, 100 nm. c, 50 nm. (d) Raman spectra of CuO and CeO_2/CuO. (e) High-resolution HAADF-STEM images of CeO_2/CuO. Scale bar, 5 nm. (f) EDS elemental mapping images of Cu, O and Ce of CeO_2/CuO. Scale bar, 100 nm. (g) XPS Cu 2p spectrum of CuO and CeO_2/CuO. (h) and (i), Cu K-edge XANES and EXAFS spectra of CuO, CeO_2/CuO, and reference samples (ref Cu, ref CuO and ref Cu_2O).

© 2025 Wiley-VCH GmbH

presence of CeO_2 nanoislands on the CuO matrix (Figure 2e), indicating the abundant interface between CeO_2 and CuO. Figure 2f shows the energy dispersive spectroscopy (EDS) elemental mapping profile, demonstrating the homogeneous distribution of Cu and Ce throughout the CeO_2/CuO catalyst. The composition of the CeO_2/CuO catalyst was also quantified by inductively coupled plasma mass spectrometry, determining a Ce/(Cu + Ce) atomic ratio of 9.3 : 100.

The electronic structures of CeO_2/CuO and CuO catalysts were comprehensively examined using X-ray photoelectron spectroscopy (XPS) and X-ray absorption spectroscopy (XAS). The XPS survey spectrum of CeO_2/CuO shows the coexistence of Cu, Ce and O elements (Figure S13). The high-resolution Cu 2p XPS spectrum of CeO_2/CuO exhibits distinct binding energies at 933.8 and 953.9 eV (Figure 2g), corresponding to $2p_{3/2}$ and $2p_{1/2}$ orbitals of Cu(II), respectively. Notably, the binding energy of the Cu 2p peak for CeO_2/CuO is positively shifted by 0.25 eV compared to pure CuO, indicating the obvious electron transfer from CuO to CeO_2. Besides, the Ce 3d spectrum shows that Ce^{4+} is the predominant chemical state of Ce (Figure S13), consistent with the presence of CeO_2. Figure 2h illustrates the normalized Cu K-edge X-ray absorption near-edge structures (XANES) of CeO_2/CuO and CuO catalysts, along with Cu foil, Cu_2O, and CuO references. Clearly, the pre-edge and white-line peak of CeO_2/CuO are very similar to those of standard CuO, confirming Cu(II) as the dominant species again. The extend X-ray absorption fine structures (EXAFS) for both CeO_2/CuO and CuO (Figure 2i) display two principal peaks: one at 1.44 Å assigned to Cu–O coordination shell, and another at 2.50 Å attributed to Cu–Cu coordination shell. Overall, we have created an inverse CeO_2/CuO catalyst featuring an abundant interface between CeO_2 nanoislands and CuO matrix. The rich interface is believed to provide the structural basis for generation of interfacial O_v-Cu pair sites under the reductive environment during ECO_2R.

Acidic ECO_2R Performance

Having established the detailed structural properties of CeO_2/CuO catalyst, the performance in acidic ECO_2R was evaluated using a homemade flow cell (Figures S14 and S15). Prior to testing, both the CeO_2/CuO and CuO catalysts were subjected to a pre-electroreduction treatment in a 0.5 M K_2SO_4 electrolyte under galvanostatic conditions. From the polarization curves for acidic ECO_2R, it is observed that the CeO_2/CuO catalyst exhibits a higher current density compared to the CuO catalyst (Figure S16 and S17). The potentiostatic electrolysis was then performed across a range of potentials from −1.0 to −1.6 V_{RHE} to assess product selectivity. As shown in Figure 3a, C_1 molecules (i.e. CO and HCOOH) are the main products over the CeO_2/CuO catalyst in the high potential region. With decreasing potential, the Faradaic efficiency of H_2 gradually decreases to 12.0 %, while the FE of C_2H_5OH significantly increases, reaching a maximum of 48.5 % at −1.5 V_{RHE}. The catholyte composition of 0.5 mM H_2SO_4 and 3 M KCl was determined by optimizing the K^+ concentration and pH (Figures S18 and S19). In contrast, the CuO catalyst exhibits significantly

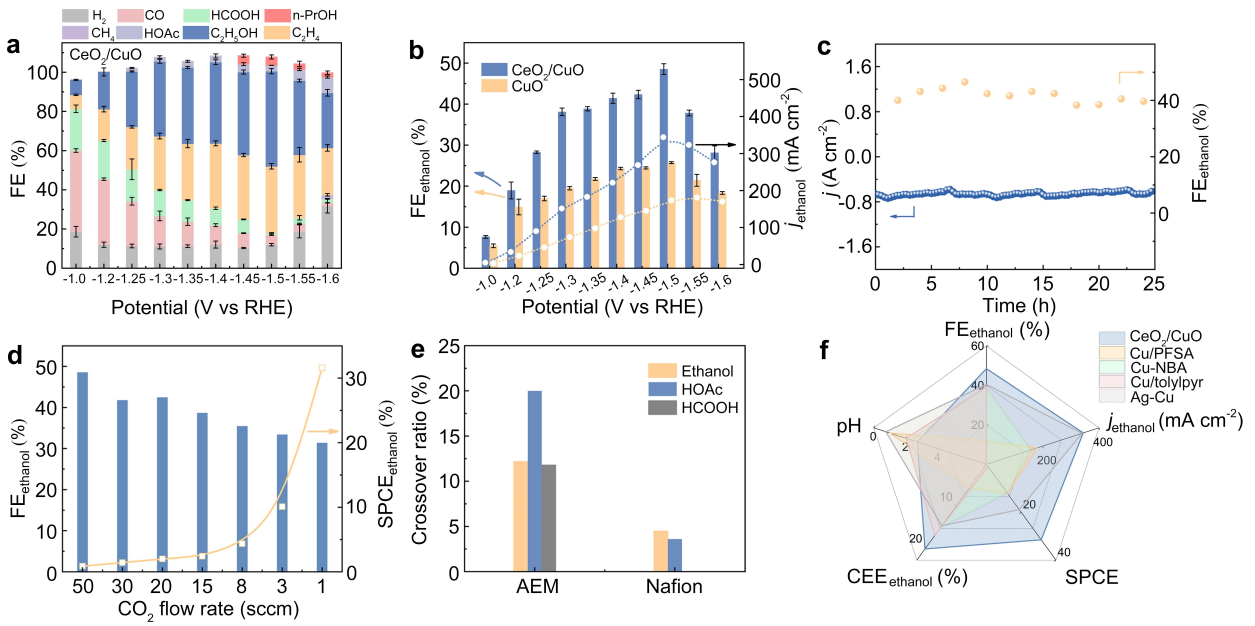

Figure 3. Acidic ECO_2R performance. (a) Potential-dependent FE of ECO_2R products on the CeO_2/CuO in acidic media of 0.5 mM H_2SO_4 and 3 M KCl in a flow cell. (b) FE and partial current density of ethanol over CeO_2/CuO and CuO. (c) Total current density and ethanol FE during long-term stability test on CeO_2/CuO at −1.53 V_{RHE}. (d) FE and SPCE of ethanol on CeO_2/CuO at various CO_2 gas flow rate. (e) Comparison for liquid products crossover in an AEM-based and Nafion-based ECO_2R flow cell assembled with CeO_2/CuO cathodic catalyst. (f) Performance comparison with recent reports on the CO_2R to ethanol in acidic media.

© 2025 Wiley-VCH GmbH

lower selectivity for ethanol, with a maximal FE of 25.7 % at −1.5 V_{RHE} (Figure 3b, Figure S20). Consistent with the trend in FEs, the ethanol partial current densities over the CeO_2/CuO catalyst are much higher than those for the CuO catalyst across all potentials, with a peak partial current density of 344.0 mA cm^{-2} achieved at −1.5 V_{RHE}. It should be emphasized that this remarkable FE for C_2H_5OH represents a record-high value for ethanol formation in acidic ECO_2R when compared to ever-reported catalysts (Table S1). Also, the CeO_2/CuO catalyst achieves a very high FE of 89.8 % for C_{2+} products at −1.5 V_{RHE}, which exceeds most of the state-of-the-art catalysts (Figure S21, Table S1). More importantly, the ratios of $FE_{ethanol}/FE_{ethylene}$ at all potentials are larger than 1.0 (Figure S22), with a maximum of 1.4 at −1.5 V_{RHE}, evidencing the more favorable formation of ethanol over ethylene on the CeO_2/CuO catalyst. As contrast, the ethylene FEs are higher than ethanol FEs at all potentials over CuO catalyst, consistent with prior studies.[18] These results well reproduce the DFT predictions, hinting the successful construction of interfacial O_v-Cu pair sites on the CeO_2/CuO catalyst.

The catalytic stability of the CeO_2/CuO catalyst was also assessed. Clearly, both the FE and partial current density for ethanol production on the CeO_2/CuO catalyst show negligible decay over 25 h (Figure 3c). TEM analysis indicates that the leaf-shaped nanosheet morphology is preserved after the stability test (Figure S23). XRD and Raman analyses further confirm that the CeO_2 is also remained (Figure S23). We then evaluated the single-pass carbon efficiency (SPCE) of the CeO_2/CuO catalyst at various CO_2 flow rates in acidic medium (Figure 3d). The SPCE of ethanol reaches a maximal value of 31.5 % by reducing the CO_2 flow rate from 50 to 1 sccm. This value represents the highest carbon efficiency for ethanol production to date, surpassing the theoretical maximum efficiency (~25 %) in alkaline environments, thus underscoring the advantage of acidic ECO_2R. Furthermore, we compared liquid product crossover in our Nafion-based electrolyzer with an anion exchange membrane (AEM)-based electrolyzer to highlight the advantage of acidic ECO_2R in mitigating the issue of liquid product crossover in traditional AEM-based cells.[4] As depicted in Figure 3e, in an AEM-based electrolyzer, crossover of liquid product was determined as 11.8 % for formate, 20.0 % for acetate, and 12.2 % for ethanol within 1,400 s electrolysis at a current density of 400 mA cm^{-2}. In contrast, in our Nafion 117-based acidic CO_2 flow cell, the cross-reactivity of ethanol and acetic acid into the anolyte is as low as 4.5 % and 3.6 %, respectively, with no formate detected. With all these metrics measured above, comprehensive comparisons were conducted for the CeO_2/CuO catalyst and those state-of-the-art catalysts. Among all reported catalysts to date, the as-designed CeO_2/CuO catalyst shows the highest $FE_{ethanol}$ and partial current density for ethanol production, along with the encouraging SPCE of 31.5 % and cathode energy efficiency (CEE) of 20.3 % (Figure 3f, Table S1). These metrics rank it as the best catalyst for ethanol production in acidic ECO_2R.

Spectroscopic Studies

As discussed above, a favored reaction pathway toward ethanol over ethylene pathway in ECO_2R occurs on the CeO_2/CuO, which reproduces our DFT calculations. To experimentally validate the DFT calculations, we performed a series of spectroscopic studies. The chemical state of the as-prepared catalysts under ECO_2R conditions was initially probed using in situ XAS. These XANES spectra were recorded at OCP and −1.5 V_{RHE} using a custom-built flow cell (Figure S24). The results show that the absorption edges of both the CeO_2/CuO and CuO catalysts are nearly identical to that of metallic copper (Cu^0) at −1.5 V_{RHE} (Figure 4a and Figure S25). Also, the Fourier-transformed Cu K-edge EXAFS spectra and the wavelet transform (WT)-EXAFS spectra of the two catalysts can be well assigned to the coordination of Cu–Cu (Figure 4b, Figures S26 and Figure S27). These observations evidence that the CuO phase in two catalysts can be reduced to metallic Cu at −1.5 V_{RHE}, indicating that Cu^0 is the active phase for ECO_2R in these two catalysts. While a few previous studies reported that CeO_2 can induce the high-valent Cu^+ sites,[19] our findings suggest the dominant role of metallic Cu sites in promoting ethanol production.

To monitor the actual chemical structure of the catalyst under the ECO_2R conditions, we also employed in situ Raman spectroscopy with a 488 nm laser excitation (Figure 4c, Figures S28 and S29). The characteristic CuO signals at 280, 329, and 612 cm^{-1} disappear for both CeO_2/CuO and CuO catalysts, indicating the complete transformation of CuO to metallic Cu. Also, the F_{2g} symmetric stretching mode of Ce–O bonds at approximately 460 cm^{-1} across various applied potentials can be observed for CeO_2/CuO catalyst, demonstrating that CeO_2 can be well preserved during the reduction process. Additionally, a new peak at ~590 cm^{-1}, corresponding to the O_v,[20] appears at the negative potentials, with increasing O_v intensity as the potential becomes more negative. This result manifests that the O_v in CeO_2 nanoislands can be stimulated under the negative reduction potential. With the generation of O_v in CeO_2 nanoislands, it is expected that a part of Ce^{4+} would be reduced into Ce^{3+}, which was monitored by the XPS technique. Consistent with the observations in in situ Raman spectra, the relative fraction of Ce^{3+} in the CeO_2/CuO catalyst progressively increases from 4.1 % at OCP to 11.0 % at −1.0 V_{RHE}, 21.4 % at −1.25 V_{RHE}, and 36.8 % at −1.50 V_{RHE} (Figure S30). Overall, the combined in situ XAS, Raman spectroscopy, and ex situ XPS characterization results corroborate that the CeO_2/Cu with abundant O_v in CeO_2 nanoislands is the actual catalyst for ECO_2R. Given the co-existence of abundant O_v and CeO_2-Cu interface, it is reasonable to conclude that numerous O_v-Cu pair sites are formed in the catalyst. These O_v-Cu pair sites offer the active sites for preferential ethanol production in the CeO_2/CuO catalyst, as suggested by our DFT calculations.

To further validate the catalytic mechanism proposed by DFT calculations, we investigated the adsorption of key species in ECO_2R on the catalysts. Firstly, CO_2 temperature-programmed desorption (TPD) was employed to analyze

 © 2025 Wiley-VCH GmbH

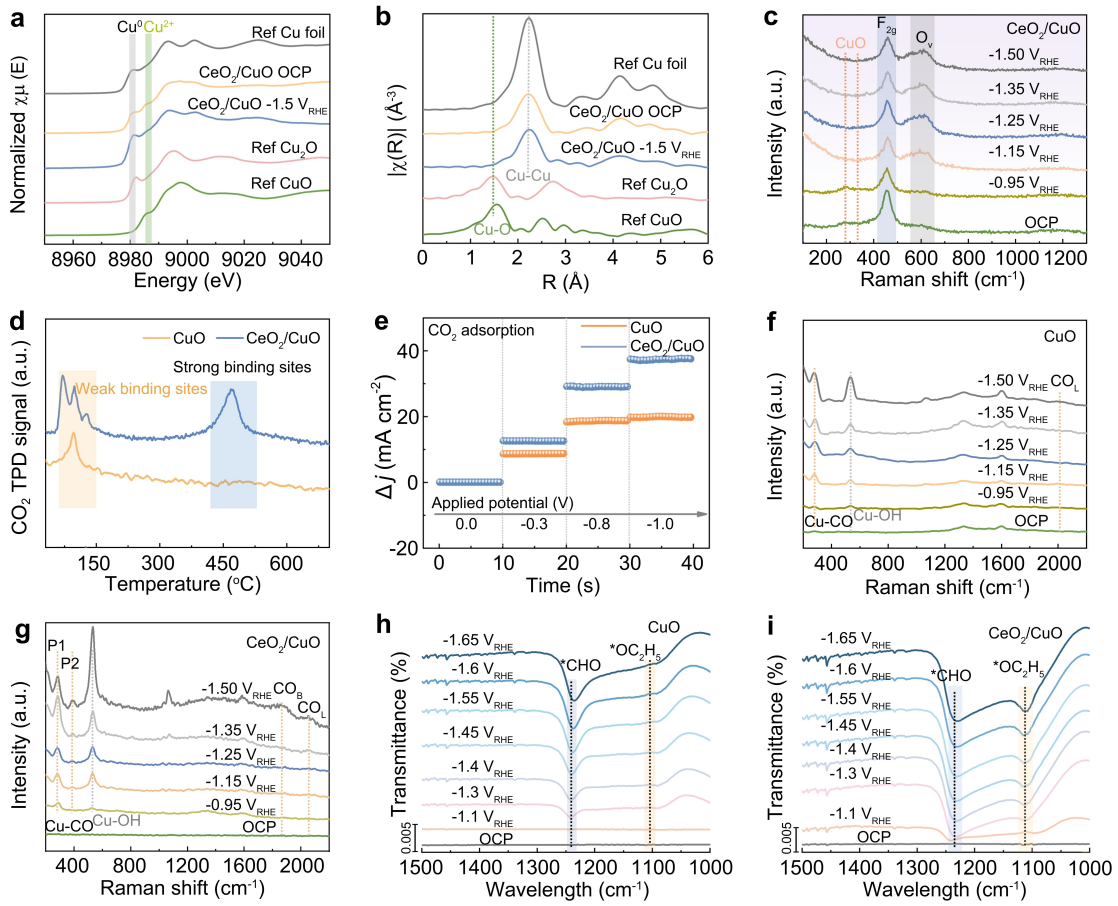

Figure 4. Spectroscopic evidence. (a) Cu K-edge XANES spectra for CeO_2/CuO under OCP and at −1.5 V_{RHE}. (b) Corresponding EXAFS spectra for CeO_2/CuO at OCP and −1.5 V_{RHE}. (c) In situ Raman spectra of CeO_2/CuO as a function of applied potential using 488 nm excitation light. (d) CO_2 TPD curves of the CuO and CeO_2/CuO catalysts. (e) CO_2 adsorption responses for CuO and CeO_2/CuO under different applied voltages. (f) and (g) In situ Raman spectra showing the adsorption of key intermediates on CuO and CeO_2/CuO under different applied potentials using 633 nm excitation light. (h) and (i) In situ ATR-SEIRAS spectra of CuO and CeO_2/CuO during acidic ECO_2R.

the CO_2 adsorption strength on CeO_2/CuO and CuO catalysts. For the CuO catalyst, CO_2 desorption peaks below 100°C are observed (Figure 4d). In contrast, the CeO_2/CuO catalyst exhibits an additional desorption peak in the temperature range of 400–540°C, manifesting the presence of strong-binding sites for CO_2. We speculate the O_v in CeO_2 nanoislands could act as the strong-binding sites for CO_2 as predicted by the DFT calculations, which is also supported by prior studies.[21] Further investigation into CO_2 adsorption and activation was conducted using gas electro-response experiments (Figure S31). The result demonstrates an enhanced CO_2 adsorption response on CeO_2/CuO catalyst compared to CuO catalyst due to the strengthened CO_2 adsorption and activation for the former (Figure 4e). This result is in accordance with the DFT calculations which show a stronger capability for CO_2 adsorption and activation for O_v in CeO_2 nanoislands.

We also used the in situ Raman technique with a 633 nm laser excitation to probe the adsorption of key intermediates on the CeO_2/CuO and CuO catalysts at different operated potentials (Figure 4f, g). Two distinct bands at ~286 cm^{-1} and ~390 cm^{-1} are assigned to the restricted rotation of *CO (P1) and Cu-CO stretching (P2), respectively. Compared to the CuO catalyst, the CeO_2/CuO catalyst features a larger P2/P1 ratio at a corresponding potential, indicating the higher *CO coverage and stronger *CO adsorption on the CeO_2/CuO catalyst. Furthermore, the Raman spectra for the CeO_2/CuO catalyst show both mixed atop-bound CO (CO_{atop}) and bridge-bound CO (CO_{bridge}) configurations. This is in contrast to the CuO catalyst, where the C=O stretching band primarily arises from CO_{atop}. These observations consistently indicate the increased *CO coverage and strengthened *CO adsorption on the CeO_2/CuO catalyst, in agreement with the DFT calculations that show a much lower formation energy of *CO on the interfacial O_v-Cu pair sites.

We further performed in situ attenuated total reflectance-surface enhanced infrared absorption spectroscopy (ATR-SEIRAS) to examine the adsorption of key intermediates on CeO_2/CuO and CuO catalysts (Figure S32). The peaks in the ATR-SEIRAS spectra were assigned to the corresponding intermediates based on previous studies (Table S2).[22] Consistent with the observations in in situ Raman spectra, the increased *CO coverage can be identi-

© 2025 Wiley-VCH GmbH

fied on the CeO_2/CuO catalyst, where the intensified linearly bonded *CO adsorption peak (~2080 cm^{-1}) is observed relative to that on the CuO catalyst (Figure S33). In addition, the features of *CHO and *OC_2H_5 at 1230 cm^{-1} and ~1115 cm^{-1} are observed on both CeO_2/CuO and CuO catalysts (Figure 4h,i), which are the key intermediates for CO_2-to-ethanol pathway. Clearly, the CeO_2/CuO catalyst shows significantly enhanced *CHO and *OC_2H_5 intensities compared to CuO, well consistent with the increased ethanol productivity. Taken together, these spectroscopic studies on the CeO_2/CuO catalyst evidence the presence of O_v-Cu pair sites and the strengthened adsorption of *CO_2, *CO, and *CHO intermediates, well consistent with the DFT calculations.

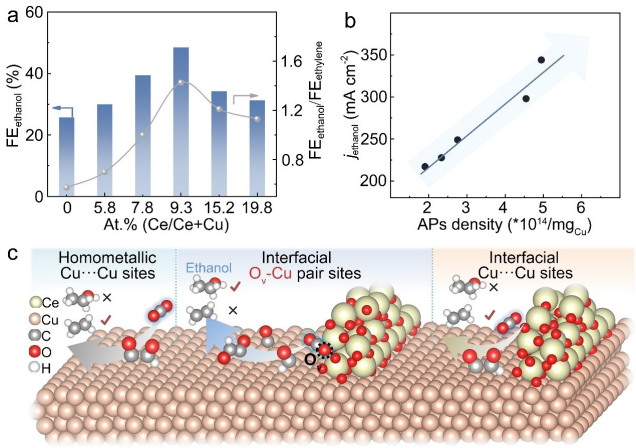

Figure 5. Correlation between the density of interfacial O_v-Cu pair sites and CO_2-to-ethanol activity. (a) Comparison of the $FE_{ethanol}$ and the ratio of $FE_{ethanol}$ to $FE_{ethylene}$ on CeO_2/CuO with increasing CeO_2 ratio at −1.5 V_{RHE}. (b) Specific activity for ethanol production plotted against the active O_v-Cu pair sites (APs) density. (c) Schematic illustrating enhanced ethanol generation over asymmetric O_v-Cu sites, with conventional homometallic Cu···Cu sites and interfacial Cu···Cu sites for comparison. Yellow, pink, gray, red, and white spheres in the model represent Ce, Cu, C, O, and H atoms, respectively.

Evidencing the Active Site for Ethanol Production

To further evidence that the interfacial O_v-Cu pair sites are the active sites in the CeO_2/CuO catalyst for ethanol formation, we explored the correlation between the density of these sites and ethanol productivity. If the interfacial O_v-Cu pair sites are indeed the active sites for ethanol formation, we would expect a linear correlation between the density of these sites and ethanol productivity. Since the O_v concentration in CeO_2 nanoislands under the ECO_2R conditions is mainly determined by the reduction potential (this is also proven as above), the density of interfacial O_v-Cu pair sites is approximately proportional to the interface length at a constant reduction potential. On this basis, we regulated the density of interfacial O_v-Cu pair sites by modulating the interface length between CeO_2 nanoislands and CuO, which was achieved by altering the amount of Ce precursor in the synthesis. Specifically, inverse CeO_2/CuO catalysts with various Ce/(Cu+Ce) atomic ratios of 5.8:100, 7.8:100, 15.2:100, and 19.8:100 were prepared (Figure S12, Figure S34 and Figure S35). According to the Scherrer equation, the average size of CeO_2 nanoislands in these catalysts was further estimated from the corresponding XRD pattern, which shows the increasing size of CeO_2 nanoislands with increasing Ce content.

We further measured the difference in electrochemically active surface area of Cu between the pristine CuO catalyst and CeO_2/CuO catalyst with varying Ce content (Figure S36), from which the interface length can be derived based on a reasonable assumption that the reduced active surface area of Cu is covered by CeO_2 nanoislands (Supplementary Note 1). The result shows that the interface length initially increases with the Ce content but decreases when Ce/(Cu+Ce) atomic ratio exceeds 9.3:100 (Figure S37), which can be rationalized by the continuously increasing size of CeO_2 nanoislands. In line with the trend in the interface length, the ethanol FE and partial current density also follow a similar relationship with Ce content at −1.5 V_{RHE} (Figure 5a and Figures S38 and Figure S39), indicating a positive correlation between interface length and ethanol productivity. As the interfacial O_v-Cu pair sites are significantly more active than the interfacial Cu–Cu sites according to our DFT calculations, the correlation between interface length and ethanol productivity strongly supports that interfacial O_v-Cu pair sites are the active sites in CeO_2/CuO catalysts.

We further quantitatively calculated the density of active O_v-Cu pair sites (APs) for the catalysts with varying Ce contents and correlated the density of APs with ethanol productivity. As the interfacial Cu density is far in excess relative to interfacial O_v density, the density of O_v-Cu pair sites hinges on the interfacial O_v density, which can be derived from the interface length and the probability of O_v (see Supplementary Note 2). The probability of O_v for the CeO_2/CuO catalysts with varying interface lengths under the ECO_2R conditions was then evaluated by ex situ XPS technique. It is found that all these CeO_2/CuO catalysts have a very close O_v probability of 18.4% under −1.5 V_{RHE} (Figure S40). Based on the estimated interface length and O_v probability, the density of O_v-Cu pair sites was then derived for the CeO_2/CuO catalysts with different Ce contents, which was further correlated to the ethanol partial current density (Figure 5b). An approximately linear correlation between the density of O_v-Cu pair sites and ethanol productivity is evident, strongly supporting that the interfacial O_v-Cu pair sites are the active sites in CeO_2/CuO catalysts for ethanol production. Altogether, relative to Cu sites on the Cu (111) surface and Cu sites near the CeO_2/CuO interface, the interfacial O_v-Cu pair sites are revealed to preferentially promote the ethanol over ethylene production through the interfacial O_v-involved mechanism (Figure 5c), which significantly favors the *CO/*CHO formation, asymmetric CHO-CO coupling, and *CH_2CHOH stabilization.

© 2025 Wiley-VCH GmbH

Conclusion

In summary, we have demonstrated that interfacial O_v-Cu pair sites are the active sites on inverse CeO_2/Cu catalysts that enable efficient CO_2 electroreduction to ethanol in acidic conditions. A linear correlation between the density of O_v-Cu pair sites and ethanol productivity on the inverse CeO_2/Cu catalysts was evidenced, strongly supporting their role as active sites. Moreover, a record-high FE of 48.5 % and a partial current density of 344.0 mA cm^{-2} for ethanol production were achieved over the inverse CeO_2/Cu catalyst with the highest density of O_v-Cu pair sites in acidic electrolyte. Mechanistic studies combining DFT calculations with spectroscopic techniques indicate an O_v-involved mechanism where interfacial O_v sites directly activate and dissociate CO_2 into *CO in a thermodynamically spontaneous manner, thus favoring the *CHO formation and asymmetric CHO-CO coupling. Furthermore, the asymmetric O_v-Cu pair sites could preferentially stabilize the *CH_2CHOH intermediate, resulting in the more favorable production of ethanol over ethylene. Beyond presenting a remarkable electrocatalyst for ethanol electrosynthesis in an acidic ECO_2R system, our findings pave the way for the rational design of advanced catalysts, offering profound implications for future research in catalysis and sustainable energy production.

Acknowledgements

This work was supported by NSFC (No. 22322902, U22A20396, and 22211540385), the National Key Research and Development Program of China (No. 2021YFA1502000), the Science and Technology Innovation Program of Hunan Province (No. 2021RC3065), the Jiebang Guashuai Project of Changsha City (No. kq2301009), Guangdong Basic and Applied Basic Research Foundation (No. 2024A1515012350), Postgraduate Scientific Research Innovation Project of Hunan Province (No. CX20230455), and the Shenzhen Science and Technology Program (No. JCYJ20210324120800002, JCYJ20220818100012025, and JCYJ20230807122007015). The authors acknowledge financial support from the Innovation and Technology Commission for MOST-ITC Joint Funding Scheme (Grant no. MHP/104/21). The XAFS measurements were performed at BL11B beamline of Shanghai Synchrotron Radiation Facility (SSRF). Supercomputing facilities were provided by Hefei Advanced Computing Center and Computing Center in Xi′an. The authors are grateful for resources from the Analytical Instrumentation Center of Hunan University for the Raman measurements.

Conflict of Interest

The authors declare no conflict of interest.

Data Availability Statement

Research data are not shared.

Keywords: Acidic CO_2 electroreduction · ethanol · oxygen vacancy · pair sites · catalytic mechanism

[1] a) H. Zhang, J. Gao, D. Raciti, A. S. Hall, *Nat. Catal.* **2023**, *6*, 807–817; b) H. Wu, L. Huang, J. Timoshenko, K. Qi, W. Wang, J. Liu, Y. Zhang, S. Yang, E. Petit, V. Flaud, J. Li, C. Salameh, P. Miele, L. Lajaunie, B. Roldán Cuenya, D. Rao, D. Voiry, *Nat. Energy* **2024**, *9*, 422–433; c) J. Zhang, G. Zeng, L. Chen, W. Lai, Y. Yuan, Y. Lu, C. Ma, W. Zhang, H. Huang, *Nano Res.* **2022**, *15*, 4014–4022; d) T. Yang, M. Kuang, J. Yang, *Chin J. Struct. Chem.* **2024**, *43*, 100350.

[2] a) J. E. Huang, F. Li, A. Ozden, A. Sedighian Rasouli, F. P. García de Arquer, S. Liu, S. Zhang, M. Luo, X. Wang, Y. Lum, Y. Xu, K. Bertens, R. K. Miao, C.-T. Dinh, D. Sinton, E. H. Sargent, *Science* **2021**, *372*, 1074–1078; b) Y. Qiao, W. Lai, K. Huang, T. Yu, Q. Wang, L. Gao, Z. Yang, Z. Ma, T. Sun, M. Liu, C. Lian, H. Huang, *ACS Catal.* **2022**, *12*, 2357–2364; c) Z. Ma, Z. Yang, W. Lai, Q. Wang, Y. Qiao, H. Tao, C. Lian, M. Liu, C. Ma, A. Pan, H. Huang, *Nat. Commun.* **2022**, *13*, 7596; d) H. Liu, T. Yan, S. Tan, L. Sun, Z. Zhang, S. Hu, S. H. Li, X. Kang, Y. Lei, L. Jiang, T. Hou, L. Liu, Q. Yu, B. Liu, *J. Am. Chem. Soc.* **2024**, *146*, 5333–5342.

[3] a) M. Fan, J. E. Huang, R. K. Miao, Y. Mao, P. Ou, F. Li, X.-Y. Li, Y. Cao, Z. Zhang, J. Zhang, Y. Yan, A. Ozden, W. Ni, Y. Wang, Y. Zhao, Z. Chen, B. Khatir, C. P. O'Brien, Y. Xu, Y. C. Xiao, G. I. N. Waterhouse, K. Golovin, Z. Wang, E. H. Sargent, D. Sinton, *Nat. Catal.* **2023**, *6*, 763–772; b) Y. Cao, Z. Chen, P. Li, A. Ozden, P. Ou, W. Ni, J. Abed, E. Shirzadi, J. Zhang, D. Sinton, J. Ge, E. H. Sargent, *Nat. Commun.* **2023**, *14*, 2387; c) W. Lai, Y. Qiao, Y. Wang, H. Huang, *Adv. Mater.* **2023**, *35*, e2306288.

[4] Y. Xie, P. Ou, X. Wang, Z. Xu, Y. C. Li, Z. Wang, J. E. Huang, J. Wicks, C. McCallum, N. Wang, Y. Wang, T. Chen, B. T. W. Lo, D. Sinton, J. C. Yu, Y. Wang, E. H. Sargent, *Nat. Catal.* **2022**, *5*, 564–570.

[5] a) M. Fan, R. K. Miao, P. Ou, Y. Xu, Z. Y. Lin, T. J. Lee, S. F. Hung, K. Xie, J. E. Huang, W. Ni, J. Li, Y. Zhao, A. Ozden, C. P. O′Brien, Y. Chen, Y. C. Xiao, S. Liu, J. Wicks, X. Wang, J. Abed, E. Shirzadi, E. H. Sargent, D. Sinton, *Nat. Commun.* **2023**, *14*, 3314; b) X. Zi, Y. Zhou, L. Zhu, Q. Chen, Y. Tan, X. Wang, M. Sayed, E. Pensa, R. A. Geioushy, K. Liu, J. Fu, E. Cortes, M. Liu, *Angew. Chem. Int. Ed.* **2023**, *62*, e202309351; c) S. Yu, H. Yamauchi, S. Wang, A. Aggarwal, J. Kim, K. Gordiz, B. Huang, H. Xu, D. J. Zheng, X. Wang, H. Iriawan, D. Menga, Y. Shao-Horn, *Nat. Catal.* **2024**, *7*, 1000–1009; d) Z. Huang, T. Yang, Y. Zhang, C. Guan, W. Gui, M. Kuang, J. Yang, *Chin. J. Catal.* **2024**, *63*, 61–80.

[6] a) J. Zhang, G. Zeng, S. Zhu, H. Tao, Y. Pan, W. Lai, J. Bao, C. Lian, D. Su, M. Shao, H. Huang, *Proc. Natl. Acad. Sci. USA* **2023**, *120*, e2218987120; b) Y. Zang, T. Liu, P. Wei, H. Li, Q. Wang, G. Wang, X. Bao, *Angew. Chem. Int. Ed.* **2022**, *61*, e202209629; c) M. Luo, Z. Wang, Y. C. Li, J. Li, F. Li, Y. Lum, D. H. Nam, B. Chen, J. Wicks, A. Xu, T. Zhuang, W. R. Leow, X. Wang, C. T. Dinh, Y. Wang, Y. Wang, D. Sinton, E. H. Sargent, *Nat. Commun.* **2019**, *10*, 5814; d) F. Xu, B. Feng, Z. Shen, Y. Chen, L. Jiao, Y. Zhang, J. Tian, J. Zhang, X. Wang, L. Yang, Q. Wu, Z. Hu, *J. Am. Chem. Soc.* **2024**, *146*, 9365–9374.

[7] a) Z. Liu, L. Song, X. Lv, M. Liu, Q. Wen, L. Qian, H. Wang, M. Wang, Q. Han, G. Zheng, *J. Am. Chem. Soc.* **2024**, *146*, 14260–14266; b) F. Li, Y. C. Li, Z. Wang, J. Li, D.-H. Nam, Y.

 © 2025 Wiley-VCH GmbH

Lum, M. Luo, X. Wang, A. Ozden, S.-F. Hung, B. Chen, Y. Wang, J. Wicks, Y. Xu, Y. Li, C. M. Gabardo, C.-T. Dinh, Y. Wang, T.-T. Zhuang, D. Sinton, E. H. Sargent, *Nat. Catal.* **2019**, *3*, 75–82; c) Y. C. Li, Z. Wang, T. Yuan, D. H. Nam, M. Luo, J. Wicks, B. Chen, J. Li, F. Li, F. P. G. de Arquer, Y. Wang, C. T. Dinh, O. Voznyy, D. Sinton, E. H. Sargent, *J. Am. Chem. Soc.* **2019**, *141*, 8584–8591.

[8] a) Y. Yang, J. Zhang, Z. Tan, J. Yang, S. Wang, M. Li, Z. Su, *Angew. Chem. Int. Ed.* **2024**, *63*, e202408873; b) Y. Wu, C. Chen, S. Liu, Q. Qian, Q. Zhu, R. Feng, L. Jing, X. Kang, X. Sun, B. Han, *Angew. Chem. Int. Ed.* **2024**, *63*, e202410659.

[9] a) S. Kuang, Y. Su, M. Li, H. Liu, H. Chuai, X. Chen, E. J. M. Hensen, T. J. Meyer, S. Zhang, X. Ma, *Proc. Natl. Acad. Sci. USA* **2023**, *120*, e2214175120; b) G. Wen, B. Ren, X. Zhang, S. Liu, X. Li, E. M. Akinoglu, L. Tao, R. Feng, S. Wang, *Adv. Mater.* **2023**, e2310822; c) Y. Zhang, Y. Chen, X. Wang, Y. Feng, H. Zhang, G. Zhang, *Angew. Chem. Int. Ed.* **2023**, *62*, e202302241.

[10] A. Xu, S.-F. Hung, A. Cao, Z. Wang, N. Karmodak, J. E. Huang, Y. Yan, A. Sedighian Rasouli, A. Ozden, F.-Y. Wu, Z.-Y. Lin, H.-J. Tsai, T.-J. Lee, F. Li, M. Luo, Y. Wang, X. Wang, J. Abed, Z. Wang, D.-H. Nam, Y. C. Li, A. H. Ip, D. Sinton, C. Dong, E. H. Sargent, *Nat. Catal.* **2022**, *5*, 1081–1088.

[11] a) R. Wang, L.-Z. Dong, J.-W. Shi, M. Zhang, S.-L. Li, Y.-Q. Lan, J. Liu, *ACS Catal.* **2024**, *14*, 741–750; b) A. J. Garza, A. T. Bell, M. Head-Gordon, *ACS Catal.* **2018**, *8*, 1490–1499; c) T. Yang, Y. Zhang, Z. Huang, J. Yang, M. Kuang, *J. Mater. Chem. A.* **2024**, *12*, 20115–20120.

[12] M. Wang, H. Chen, M. Wang, J. Wang, Y. Tuo, W. Li, S. Zhou, L. Kong, G. Liu, L. Jiang, G. Wang, *Angew. Chem. Int. Ed.* **2023**, *62*, e202306456.

[13] a) G. Hou, Q. Wang, D. Xu, H. Fan, K. Liu, Y. Li, X. K. Gu, M. Ding, *Angew. Chem. Int. Ed.* **2024**, e202402053; b) A. Chen, X. Yu, Y. Zhou, S. Miao, Y. Li, S. Kuld, J. Sehested, J. Liu, T. Aoki, S. Hong, M. F. Camellone, S. Fabris, J. Ning, C. Jin, C. Yang, A. Nefedov, C. Wöll, Y. Wang, W. Shen, *Nat. Catal.* **2019**, *2*, 334–341; c) W. Yang, F. Qi, W. An, H. Yu, S. Liu, P. Ma, R. Chen, S. Liu, L.-L. Lou, K. Yu, *ACS Catal.* **2024**, *14*, 5936–5948.

[14] F. Zhang, B. Li, X. Quan, K. Wang, J. Xu, T. Wu, Z. Li, M. Yan, S. Liu, Y. He, Y. Shi, Y. Su, P. Xie, *ACS Catal.* **2024**, *14*, 7136–7148.

[15] a) H. Jiang, L. Wang, H. Kaneko, R. Gu, G. Su, L. Li, J. Zhang, H. Song, F. Zhu, A. Yamaguchi, J. Xu, F. Liu, M. Miyauchi, W. Ding, M. Zhong, *Nat. Catal.* **2023**, *6*, 519–530; b) J. Hu, L. Yu, J. Deng, Y. Wang, K. Cheng, C. Ma, Q. Zhang, W. Wen, S. Yu, Y. Pan, J. Yang, H. Ma, F. Qi, Y. Wang, Y. Zheng, M. Chen, R. Huang, S. Zhang, Z. Zhao, J. Mao, X. Meng, Q. Ji, G. Hou, X. Han, X. Bao, Y. Wang, D. Deng, *Nat. Catal.* **2021**, *4*, 242–250; c) L. Nie, D. Mei, H. Xiong, B. Peng, Z. Ren, X. I. P. Hernandez, A. DeLaRiva, M. Wang, M. H. Engelhard, L. Kovarik, A. K. Datye, Y. Wang, *Science* **2017**, *358*, 1419–1423.

[16] a) Z. Geng, X. Kong, W. Chen, H. Su, Y. Liu, F. Cai, G. Wang, J. Zeng, *Angew. Chem. Int. Ed.* **2018**, *57*, 6054–6059; b) F. Ye, S. Zhang, Q. Cheng, Y. Long, D. Liu, R. Paul, Y. Fang, Y. Su, L. Qu, L. Dai, C. Hu, *Nat. Commun.* **2023**, *14*, 2040.

[17] Y. C. Zhang, X. L. Zhang, Z. Z. Wu, Z. Z. Niu, L. P. Chi, F. Y. Gao, P. P. Yang, Y. H. Wang, P. C. Yu, J. W. Duanmu, S. P. Sun, M. R. Gao, *Proc. Natl. Acad. Sci. USA* **2024**, *121*, e2400546121.

[18] W. Zhang, C. Huang, Q. Xiao, L. Yu, L. Shuai, P. An, J. Zhang, M. Qiu, Z. Ren, Y. Yu, *J. Am. Chem. Soc.* **2020**, *142*, 11417–11427.

[19] a) Z. Yang, D. Ji, Z. Li, Z. He, Y. Hu, J. Yin, Y. Hou, P. Xi, C. H. Yan, *Small* **2023**, *19*, e2303099; b) X. Zhou, J. Shan, L. Chen, B. Y. Xia, T. Ling, J. Duan, Y. Jiao, Y. Zheng, S.-Z. Qiao, *J. Am. Chem. Soc.* **2022**, *144*, 2079–2084.

[20] a) Z. Su, X. Li, W. Si, L. Artiglia, Y. Peng, J. Chen, H. Wang, D. Chen, J. Li, *ACS Catal.* **2023**, *13*, 3444–3455; b) S. Loridant, *Cataly. Today.* **2021**, *373*, 98–111.

[21] R. Ye, L. Ma, X. Hong, T. R. Reina, W. Luo, L. Kang, G. Feng, R. Zhang, M. Fan, R. Zhang, J. Liu, *Angew. Chem. Int. Ed.* **2024**, *63*, e202317669.

[22] a) P. Wang, H. Yang, C. Tang, Y. Wu, Y. Zheng, T. Cheng, K. Davey, X. Huang, S. Z. Qiao, *Nat. Commun.* **2022**, *13*, 3754; b) W. Guo, S. Zhang, J. Zhang, H. Wu, Y. Ma, Y. Song, L. Cheng, L. Chang, G. Li, Y. Liu, G. Wei, L. Gan, M. Zhu, S. Xi, X. Wang, B. I. Yakobson, B. Z. Tang, R. Ye, *Nat. Commun.* **2023**, *14*, 7383.

Manuscript received: December 11, 2024
Accepted manuscript online: January 9, 2025
Version of record online: January 16, 2025

© 2025 Wiley-VCH GmbH